J Mater Sci (2015) 50:5389–5401
DOI 10.1007/s10853-015-9083-0

Enhanced flame retardancy of polypropylene by melamine-modified graphene oxide

Bihe Yuan[1,2] · Haibo Sheng[1] · Xiaowei Mu[1] · Lei Song[1] · Qilong Tai[1,2] · Yongqian Shi[1,2] · Kim Meow Liew[3] · Yuan Hu[1,2]

Received: 13 February 2015 / Accepted: 6 May 2015 / Published online: 14 May 2015

Abstract Graphene oxide (GO) is modified by melamine (MA) via the strong π–π interactions, hydrogen bonding, and electrostatic attraction. PP composites are prepared by melt compounding method, and GO/functionalized graphene oxide (FGO) is in situ thermally reduced during the processing. The results of scanning electron microscopy and transmission electron microscopy indicate that FGO nanosheets are homogeneously dispersed in polymer matrix with intercalation and exfoliation microstructure. The FGO/PP nanocomposite exhibits higher thermal stability and flame retardant property than those of the GO counterpart. During the thermal decomposition, the intercalated MA is condensed to graphitic carbon nitride (g-C_3N_4) in the confined micro-zone created by GO nanosheets. This in situ formed g-C_3N_4 provides a protective layer to graphene and enhances its barrier effect. The heat release rate and the escape of volatile degradation products are reduced in the FGO-based nanocomposites.

Electronic supplementary material The online version of this article (doi:10.1007/s10853-015-9083-0) contains supplementary material, which is available to authorized users.

✉ Yuan Hu
yuanhu@ustc.edu.cn

[1] State Key Laboratory of Fire Science, University of Science and Technology of China, Hefei 230026, China

[2] USTC-CityU Joint Advanced Research Centre, Suzhou Key Laboratory of Urban Public Safety, Suzhou Institute for Advanced Study, University of Science and Technology of China, Suzhou 215123, China

[3] Department of Architecture and Civil Engineering, City University of Hong Kong, Tat Chee Avenue, Kowloon, Hong Kong

Introduction

Since the discovery of graphene by Andre Geim and Konstantin Novoselov, remarkable progresses have been made in the development of this new nanomaterial. Graphene shows impressive thermal, mechanical, electron-transport, and optical properties [1]. Due to these excellent properties, graphene is regarded as a promising multifunctional nanofiller for polymers. If graphene can be well dispersed in polymer matrix, the properties of polymer nanocomposites will be greatly improved even at a low loading of graphene. Achievements of outstanding thermal and electrical conductivity, mechanical properties, and electromagnetic interference shielding function have been reported in graphene/polymer nanocomposites [2–4]. Due to its chemical inert feature, the strong van der Waals forces, and π–π attraction between the nanosheets, good dispersion of graphene in polymer matrices, especially in non-polar polymers, is challenging [5]. Considering the presence of oxygen functional groups on the nanosheets and larger interlayer spacing, graphene oxide (GO) is commonly used as the starting material for fabrication of graphene-based polymer nanocomposites. To make full use of GO as a reinforcing nanofiller, surface modification is necessary to improve the dispersion and control the interfacial structure. The modification of GO is mainly classified into two categories: covalent and non-covalent strategy [6]. Covalent functionalization of graphene can be realized by grafting modifiers via the reactions with the oxygen-containing functional groups [6, 7]. In the non-covalent strategy, the modifier is absorbed onto the nanosheets via various interactions, such as π–π stacking, van der Waals interactions, and electrostatic attraction [8]. Compared to the covalent method, non-covalent approach is simpler, and the original chemical structure of graphene is preserved.

Due to the marked discrepancy in polarity and compatibility, it is relatively difficult to achieve homogeneous dispersion of GO/graphene in non-polar polymers, such as polypropylene (PP) [9]. Commonly, maleic anhydride-grafted polypropylene (MAPP) is utilized to improve the compatibility between GO/graphene and PP matrix. Thus, the agglomeration of graphene is retarded to a certain degree. During melt blending process, GO undergoes thermal reduction and part of the oxygen functional groups are removed [10]. This removal of the oxygenated groups in GO is expected to weaken the interactions with MAPP, and it becomes a hurdle in improving the dispersion [8].

Analogous to montmorillonite, the features of high aspect ratio, high specific surface area, and two-dimensional nanostructure enable graphene to be a promising candidate flame retardant for polymers. Some research has already been conducted into the fire behavior of polymer/graphene nanocomposites, including charring and non-charring polymers [11–14]. The incorporation of GO, graphene, and their derivatives exerts a marked influence on the combustion behavior of polymer nanocomposites. Compared to neat polymers, the combustion heat release of graphene-based nanocomposites is reduced and their flame resistance is improved. As with other nanofillers, the uniform dispersion of graphene is crucial for enhancing the flame retardant property of polymers [12]. Schartel et al. discovered that the well-exfoliated graphene exhibits more marked flame retardant efficiency than carbon black, expanded graphite, and multiwall carbon nanotube [15, 16]. Guo et al. reported that the enhanced flame retardancy of polyethylene (PE) by graphene nanoplatelet is attributed to its tortuous pathway effects [17]. The well-dispersed graphene can work as an anti-dripping agent and increase the melt viscosity of polymer composites [15, 16, 18]. Graphene has been employed as a synergist with conventional flame retardants and nanoparticles, such as intumescent flame retardant, magnesium hydroxide, and carbon black [19–21].

For the non-charring polymers, such as PP and PE, the formation of residual inorganic carbonaceous protection layer is widely acknowledged as the main flame retardant mechanism of polymer nanocomposites [22–24]. This protective layer can act as a barrier against heat transport, which will reduce the heat transfer and the mass loss rate of polymers [22, 23]. Furthermore, the residual layer also plays the physical barrier role to mass transport and delays the escape of volatile degradation products and oxygen diffusion [14]. Thus, the barrier function of polymer nanocomposites plays a key role in the enhancement of flame retardant property. During thermal treatment or decomposition, the labile oxygen functional groups in GO are easily removed as the gas products of CO and CO_2, leaving structural defects within the nanosheets [25]. These defects will give rise to the weakened barrier performance of graphene [26]. To address this shortcoming, coating GO nanosheets with protective layer is required to improve its char barrier effect.

In this study, functionalized graphene oxide (FGO) was prepared via a non-covalent approach and was incorporated into PP matrix by melt mixing method. The dispersion state of FGO in PP is compared with that of GO/PP composite. Thermal stability and flame retardant property of the PP composites are studied, and the detailed analysis of the mechanisms is reported.

Experimental

Materials

Graphite powder (SP) and melamine (MA, AR) were purchased from Sinopharm Chemical Reagent Co., Ltd. PP (copolymer, Yungsox 3015), with a density of 0.90 g/cm^3 and a melt flow index (MFI) of 2.0 g/10 min (230 °C, 2.16 kg, ISO 1133), was supplied from Formosa Plastics Polypropylene (Ningbo) Co., Ltd. MAPP, with an MFI of 51.0 g/10 min (230 °C, 2.16 kg, ISO 1133) and 0.8 wt% of maleic anhydride, was kindly provided by Suzhou Enhand New Materials Co., Ltd.

Sample preparation

FGO synthesis

GO was prepared by oxidation of graphite powder using the modified Hummers method [27, 28]. 0.6 g of GO was dispersed in 600 mL of deionized water with continuous stirring and ultrasonication for 30 min. Then, 3 g of MA was slowly added to the GO dispersion, and the mixture was stirred at 60 °C for 10 h. The final product, FGO, was collected by centrifugation, washed with hot water, and dried at 60 °C for 24 h.

Preparation of PP composites

PP composites were prepared by melt mixing in a two-roller mill. The loading of MAPP was maintained at 5 wt% in all samples. The resin was dried at 80 °C for 12 h to remove moisture. The mixing of nanofillers and resin was conducted at 185 °C for 12 min, with a roller speed of 50 rpm. PP composites containing 0.5, 1.0, and 2.0 wt% FGO were designated as 0.5 FGO/PP, 1 FGO/PP, and 2 FGO/PP, respectively. A control composite sample with 2 wt% GO was also prepared and named as 2 GO/PP. The sheets for further characterization were prepared by

compression molding the melt-mixed samples in a press vulcanizer under 10 MPa and 190 °C.

Characterization

X-ray diffraction (XRD) pattern was collected with a Rigaku TTR-III X-ray diffractometer with Cu Kα radiation ($\lambda = 0.1542$ nm). Fourier transform infrared (FTIR) spectrum was recorded on a Nicolet 6700 spectrophotometer over the wavenumber range of 4000–500 cm^{-1} at 16 scans with a resolution of 4 cm^{-1}. X-ray photoelectron spectroscopy (XPS) measurement of the samples was done on a Thermo VG ESCALAB 250 electron spectrometer with an Al Kα line as the X-ray source (1486.6 eV). The graphitic structure of the carbonaceous materials was characterized by Raman spectroscopy, using a LABRAM-HR laser confocal microRaman spectrometer equipped with a 514.5 nm laser source. Thermogravimetric analysis (TGA) was conducted on a TA Q5000IR thermo-analyzer under N_2/air flow, with a temperature scan rate of 20 °C/min. Tapping-mode atomic force microscopy (AFM) analysis was performed on a Veeco DI Multimode V scanning probe microscope. The GO and FGO aqueous dispersions were deposited on a freshly cleaved mica surface and were dried under ambient conditions. Transmission electron microscopy (TEM) was used to image the morphology of the nanomaterials. The samples were prepared by dripping the aqueous dispersions on copper TEM grids. The Brunauer–Emmett–Teller (BET) surface area of GO and FGO was determined by N_2 adsorption at liquid nitrogen temperature, using a Micromeritics Tristar II 3020 M automatic surface area and pore analyzer. Prior to the adsorption tests, the samples were degassed at 150 °C for 5 h. TEM was also used to assess the dispersion quality of GO/FGO in PP matrix. The PP composite sheets were microtomed to ultrathin slices with a thickness of 20–100 nm using a Cambridge ultratome, and the slices were transferred onto copper grids for TEM observation. The TEM images were collected using a JEOL JEM-2100F microscope with an acceleration voltage of 200 kV. Scanning electron microscopy (SEM) images of the surface of the cryogenically broken composites were taken by an FEI Sirion 200 scanning electron microscope at an acceleration voltage of 5 kV. Prior to the tests, the fracture surface of the samples were sputter-coated with conductive layer. Thermogravimetric analysis–infrared spectrometry (TG-IR) was performed on a TGA Q5000IR thermo-analyzer which was interfaced to a Nicolet 6700 spectrophotometer. The samples were heated at a rate of 20 °C/min under N_2 atmosphere. Combustion properties of PP and its composites under forced-flaming conditions were evaluated by an FTT cone calorimeter according to ISO 5660. The samples with dimensions of 100 × 100 × 3 mm^3 were wrapped in an aluminum foil and burned under 35 kW/m^2 external heat flux.

Results and discussion

Due to the powerful π–π interactions, hydrogen bonding, and electrostatic interactions, MA exhibits strong affinity for GO [29–31]. MA can be intercalated into the interlayer region of GO, and its surface characteristic is modified. Figure 1a shows the XRD patterns of GO and FGO. The interlayer spacing of GO can be calculated from its (002) reflection peak. Upon modification, this characteristic peak shifts from 11.4° to 9.8°, indicating the enlargement of interlayer spacing from 0.776 to 0.903 nm. The increase in interlayer spacing is due to the intercalation of MA molecules. The intensity of the FGO (002) peak greatly reduces, indicating the decrease in ordered arrangement of GO after the modification. Furthermore, no peaks attributing to MA can be observed in the FGO XRD pattern. The chemical structure of GO and FGO was studied with FTIR spectroscopy, as shown in Fig. 1b. The virgin GO presents the peaks of oxygen-containing functional groups at approximately 1725, 1407, 1226, and 1092 cm^{-1}, which are ascribed to C=O stretching, O–H deformation, C–O–C stretching, and C–OH stretching vibrations, respectively [32]. The band at 1622 cm^{-1} should be assigned to the physically absorbed water or the vibration of aromatic rings [32]. In the MA FTIR spectrum, the bands at 3000–3500 and 1653 cm^{-1} are associated with the NH_2 groups [33]. The peaks at 1551, 1467, 1437, and 814 cm^{-1} are attributed to 1, 3, 5-s-triazine rings [33]. The band at 1026 cm^{-1} corresponds to C–N stretching vibration mode of MA [33]. From the FGO FTIR spectrum, it can be discerned the presence of GO and MA in FGO, due to the appearance of these characteristic peaks. It is apparent that the peaks of NH_2 groups in MA and OH groups in GO evolve into a broad band at around 3300 cm^{-1}, and the peak of NH_2 deformation red shifts to 1624 cm^{-1}. These phenomena are due to the hydrogen bonding interactions between GO and MA molecules. The absence of C=O stretching band in FGO spectrum may be the result of electrostatic interactions between GO and MA [34]. Meanwhile, the alkaline feature of MA may result in the removal of carboxyl groups and partial reduction of GO [35].

Raman spectroscopy is widely employed to investigate the structure of carbonaceous materials. The corresponding Raman spectra of GO and FGO are presented in Fig. 2a. Both GO and FGO exhibit two strong peaks at approximately 1350 and 1600 cm^{-1}, namely D and G bands, respectively. The relative intensity ratio of D and G bands (I_D/I_G) is closely related with the disorder degree of carbon

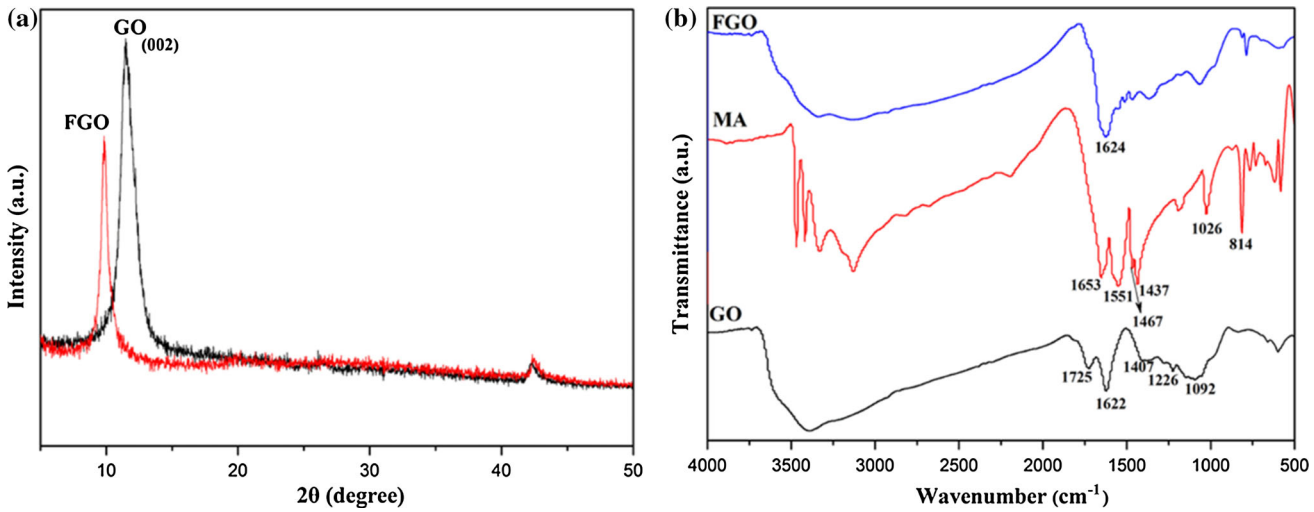

Fig. 1 **a** XRD analysis of GO and FGO; **b** FTIR spectra of GO, MA, and FGO

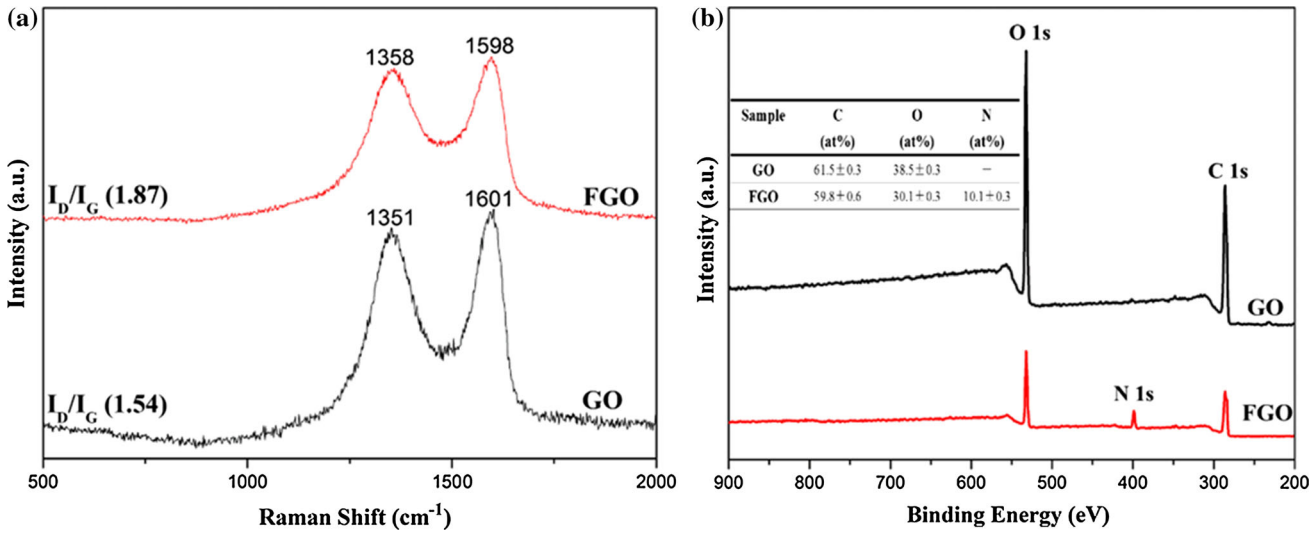

Sample	C (at%)	O (at%)	N (at%)
GO	61.5±0.3	38.5±0.3	–
FGO	59.8±0.6	30.1±0.3	10.1±0.3

Fig. 2 **a** Raman spectra and **b** XPS survey spectra of GO and FGO

materials [36]. The I_D/I_G of FGO (1.87) is higher than that of GO (1.54), suggesting higher disorder degree of FGO. In comparison with GO, the shifting of D and G bands is observed in the FGO Raman spectrum, due to the strong interfacial interactions between GO and MA [37]. Chemical composition analysis of the specimens was conducted by XPS. XPS spectra and the corresponding data are presented in Fig. 2b and the inset table, respectively. Both C and O elements are detected in the GO XPS spectrum, and the C/O atomic ratio of GO is calculated to be 1.60. FGO shows the characteristic N 1s peak at approximately 399 eV, and the atomic percentage of N in FGO is 10.1 ± 0.3 at.%. Given the chemical formula of MA ($C_3H_6N_6$), the calculated C/O ratio of the GO in FGO is approximately 1.82, which is greater than that of GO (1.60). It has been reported that the oxygen functional groups in GO can be easily removed in alkaline solution [35]. Thus, the MA solution in this work results in the partial reduction of GO, which is in accord with the FTIR analysis.

The morphology of GO and FGO was characterized by TEM (Fig. 3). As shown in Fig. 3a, the GO nanosheet exhibits a typical silk-like morphology with some wrinkles. In the FGO TEM image (Fig. 3b), it can be seen that the nanosheet is uniformly covered with organic materials. The thickness and lateral size of GO and FGO nanosheets were evaluated with AFM. The typical AFM images with height profiles are presented in Fig. 4. Analysis of AFM images of GO nanosheets in Fig. 4a reveals that the thickness of the nanosheets is in the range of 0.9–1.1 nm, which agrees well

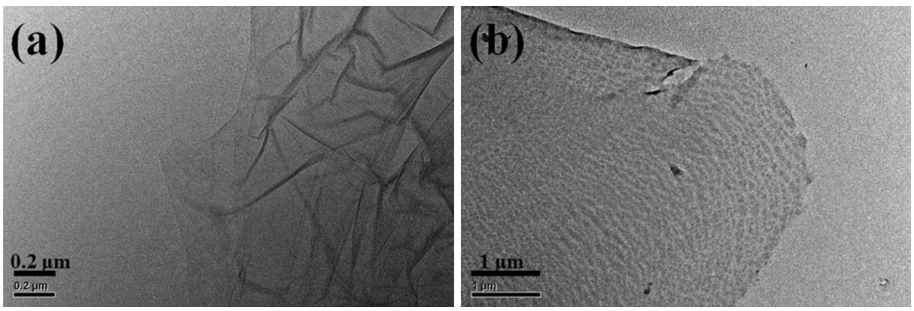

Fig. 3 TEM micrographs of **a** GO and **b** FGO

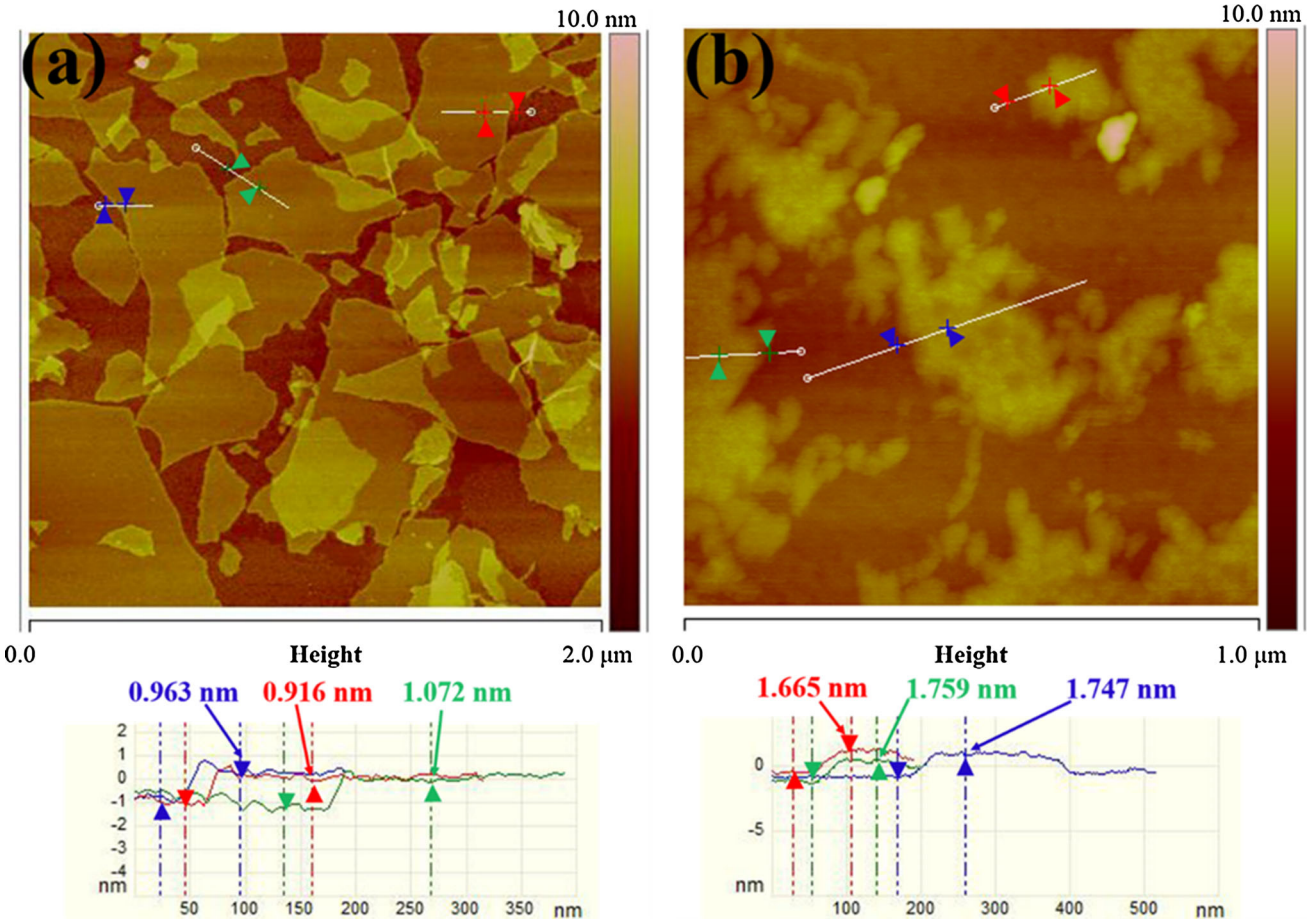

Fig. 4 AFM images of **a** GO and **b** FGO with height profiles

with the typical thickness of monolayer GO nanosheet [38], and the length varies from 0.2 to 1 μm. As shown in Fig. 4b, the FGO nanosheets have heights of around 1.7 nm, which is greater than the value of GO. This suggests that the MA molecules were uniformly coated on the GO nanosheets. The ultrasonication treatment in FGO preparation process results in the decrease in the nanosheet size [39]. Based on AFM analysis, statistical average thickness and length of GO nanosheets are approximately 1.0 nm and 0.7 μm, respectively. The average values of thickness and length of FGO nanosheets are approximately 1.7 nm and 0.4 μm, respectively. Therefore, the aspect ratios of GO and FGO nanosheets are determined to be 700 and 235, respectively. Schartel et al. explored the influence of specific surface area of carbon nanomaterials on the properties of PP composites [15]. They discovered that the specific surface area of the nanofillers exerts significant influence on the dispersion, thermal stability, and flame retardant properties of polymer [15]. The BET surface area of FGO (2.5 m^2/g) is lower than that of GO (16.6 m^2/g).

This indicates that the interlayer space of GO is blocked with the intercalated MA, and N_2 molecules are inaccessible to the interlayer area [40, 41].

Thermal stability of GO, MA, and FGO was determined with TGA under N_2 condition, and their TGA curves were plotted in Fig. 5a. GO shows a weight loss of approximately 10 % below 170 °C, due to the evaporation of residual moisture in GO. The main decomposition of GO occurs over the temperature range of 170–265 °C, which is attributed to the decomposition of the labile oxygen functional groups, such as hydroxyl and carboxyl groups [7]. The gradual removal of the thermally stable functional groups results in the slight mass loss above 265 °C. The MA exhibits a sharp weight loss between 225 and 345 °C. In this temperature range, MA easily sublimates with very little residue [42]. FGO presents a similar thermal decomposition behavior to GO. Significantly improved thermal stability is achieved for FGO as compared to that of GO. As with GO, the weight loss below 250 °C is due to the removal of water and unstable oxygen functional groups. However, the marked weight loss stage of MA is not observed in the FGO TGA curve. A gradual weight loss above 250 °C is observed in the TGA curve of FGO, predominantly due to the deoxygenation of GO and the condensation of MA. Importantly, the residual weight of FGO (54.9 wt%) at 700 °C is considerably larger than that of GO (36.2 wt%). XRD and FTIR were employed to analyze the thermal decomposition product of FGO, which was pyrolyzed in a 550 °C tubular furnace for 30 min under the protection of high-purity N_2. This pyrolysis temperature is in the temperature range of burning PP specimen during the combustion in cone calorimeter [15].

XRD pattern of the decomposed product is shown in Fig. 5b. The strong diffraction peak at approximately 27.0° is identified as the (002) plane of graphitic carbon nitride (g-C_3N_4) [43]. The FGO (002) peak at 9.8° disappears, and this peak at around 25.0° may overlap with the peak of g-C_3N_4. Furthermore, the (100) graphene plane is observed in the XRD pattern (Fig. 5b). FTIR spectrum of the decomposed product exhibits the characteristic peaks of g-C_3N_4 (Fig. 5c). The peaks in the region of 1100–1600 cm^{-1} correspond to the stretching modes of C=N and C–N heterocycles [43]. The band at 1562 cm^{-1} may also be attributed to in-plane vibrations of the sp^2-hybridized carbons in graphene [32]. The breathing mode of triazine units in g-C_3N_4 is observed at 804 cm^{-1} [43]. The broad band at approximately 3431 cm^{-1} is due to the stretching modes of terminal NH_2 or NH groups [43]. XPS survey spectrum in Fig. 5d reveals the presence of C (80.0 ± 1.7 at.%), O (5.8 ± 0.5 at.%), and N (14.2 ± 1.2 at.%) in the pyrolyzed product of FGO. Compared to FGO XPS spectrum (Fig. 2b), the decrease in oxygen content is the result of removal of the oxygen-containing groups upon thermal treatment. Figure 5e and f displays the deconvoluted C 1s

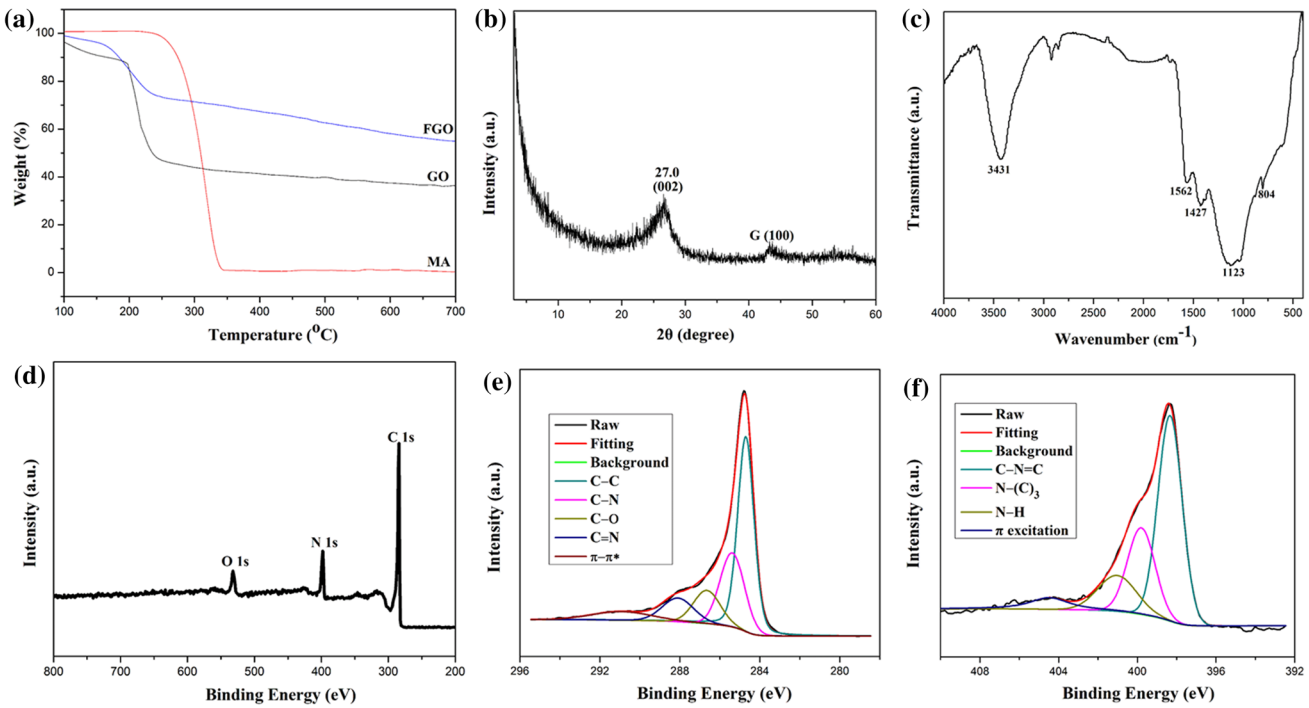

Fig. 5 **a** TGA plots of GO, MA, and FGO; **b** XRD pattern, **c** FTIR spectrum, **d** XPS survey spectrum, **e** high-resolution C 1s, and **f** N 1s XPS spectra of the pyrolyzed product of FGO

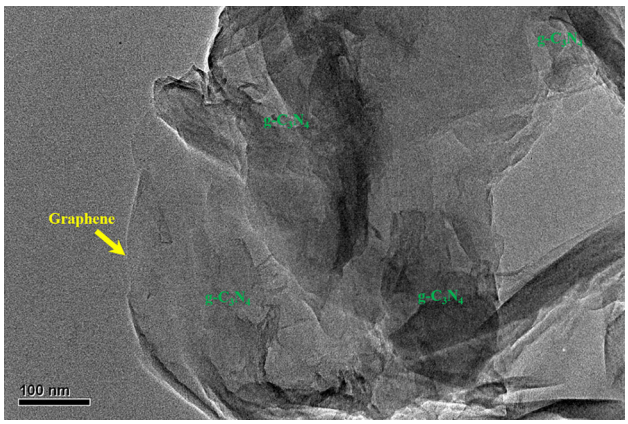

Fig. 6 TEM image of the pyrolyzed product of FGO

and N 1s spectra of the pyrolyzed product, respectively. The peaks at 284.7 and 286.7 eV are attributed to sp^2-bonded carbon and C–O groups, respectively [44]. The peaks located at 285.4 and 288.1 eV correspond to the C–N and C=N groups, respectively, in g-C_3N_4 [45]. The broad peak centered at 290.9 eV can be assigned to the characteristic π–π^* shake-up satellite peak of reduced graphene oxide [44]. Four peaks at 398.3, 399.8, 401.0, and 404.5 eV in the high-resolution N 1s XPS spectrum are attributed to the sp^2-hybridized nitrogen (C–N=C), the tertiary nitrogen bonded to carbon atoms (N–$(C)_3$), the terminal N–H groups, and π excitations [46, 47], respectively. Figure 6 shows the TEM image of the pyrolyzed product of FGO. It is apparent that the g-C_3N_4 nanosheets are attached on the graphene nanosheets. In comparison to the TEM image of FGO, the g-C_3N_4–graphene nanohybrid exhibits a more compact nanostructure, due to the coating of the in situ formed C_3N_4 nanosheets. These results confirm the thermal reduction of GO and the formation of g-C_3N_4 during the pyrolysis process.

The formation mechanism of g-C_3N_4–graphene nanohybrid is schematically presented in Fig. 7. GO is a thermally unstable material, and the oxygen functional groups can be removed at around 200 °C, yielding CO_2, CO, O_2, and water [48]. The evolution of these volatile products inevitably introduces defects and vacancies in the reduced graphene oxide nanosheets [49]. The presence of these lattice defects will weaken the barrier performance of graphene in polymer composites [26]. When MA molecules are intercalated into the layer spacing of GO, the sublimation of MA is considerably retarded in this confined micro-zone. The absorbed MA undergoes condensation to carbon nitride with the elimination of NH_3. The GO can act as a micro-reactor and carbonization template, facilitating the formation of g-C_3N_4 from the condensation of MA. The g-C_3N_4, a two-dimensional nanomaterial, possesses a similar morphology to graphene. The coating of g-C_3N_4 can act as a barrier to heat and mass transport, and it will delay the escape of volatile degradation products of GO, resulting in the improved thermal stability of FGO. The g-C_3N_4 can provide a protective layer to graphene and enhance its barrier effect. In our prior research, we found that g-C_3N_4 is completely decomposed between 600 and 700 °C in the TGA test [50]. However, marked mass loss

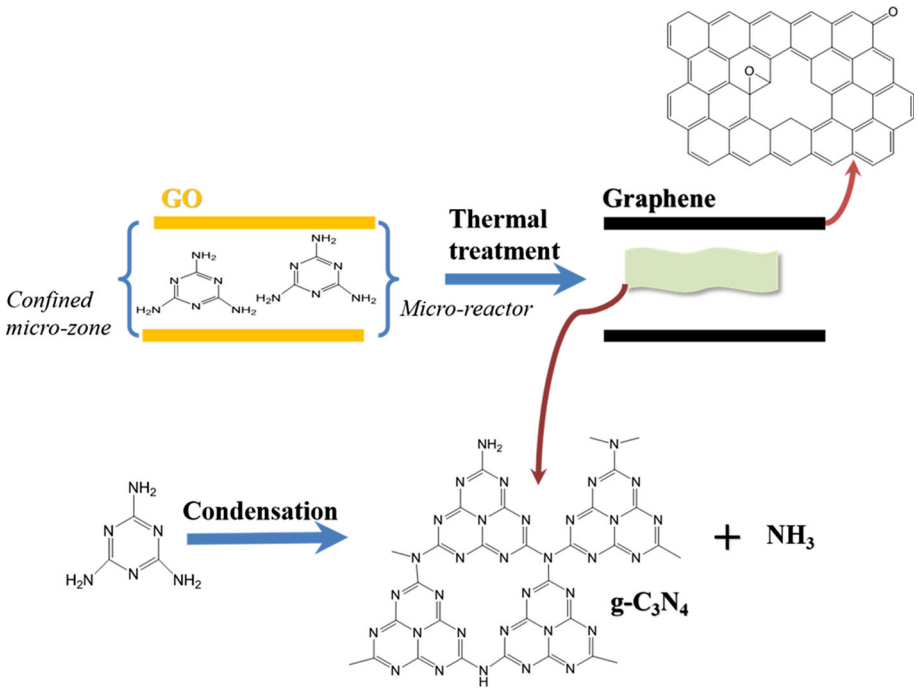

Fig. 7 Illustration of the formation of g-C_3N_4–graphene nanohybrid during the pyrolysis of FGO

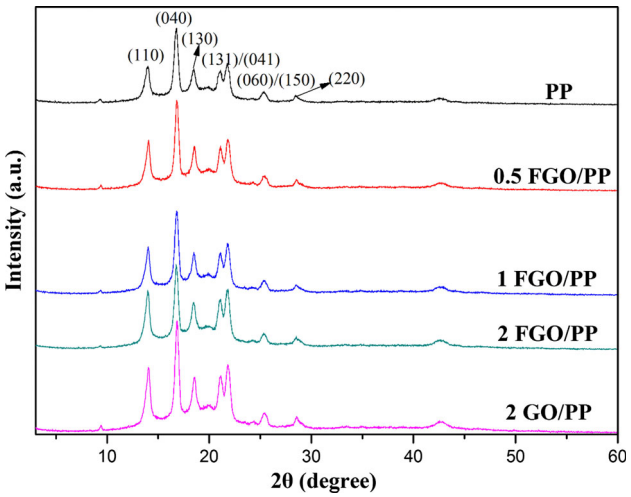

Fig. 8 XRD patterns of PP and its composites

stage at this temperature range is not observed in the TGA curve of FGO. That is to say, graphene can also protect the in situ generated g-C_3N_4 from further decomposition. The mutual protection effects of graphene and the g-C_3N_4 result in the high residual weight.

XRD is a powerful tool for characterizing the crystalline structure of polymer and evaluating the nanocomposite morphology. As shown in Fig. 8, it is clear that pure PP and its composites exhibit similar XRD patterns. (110), (040), (130), (131)/(041), (060)/(150), and (220) planes of α-crystal form of PP are observed [7]. No diffraction peak at around 10°, which is attributed to the GO (002) plane, is observed in the XRD patterns of PP composites, due to the thermal reduction of GO. During the melt blending process, part of the oxygen functional groups in GO have been removed. The (002) peak of the graphene may overlap with the (060)/(150) peak of PP.

To accurately evaluate the dispersion and morphology of graphene in PP matrix, SEM and TEM were employed. SEM images (Fig. 9) provide the dispersion information of nanomaterials at micrometer scale. As marked by an arrow, a conspicuous particle with layered structure is observed in Fig. 9a, indicating that the virgin GO nanosheets could not be effectively dispersed in the PP matrix during the melt compounding process. However, as shown in Fig. 9b, there are no agglomerates in the SEM image of 2 FGO/PP. TEM micrographs of the ultrathin slices of 2 GO/PP and 2 FGO/

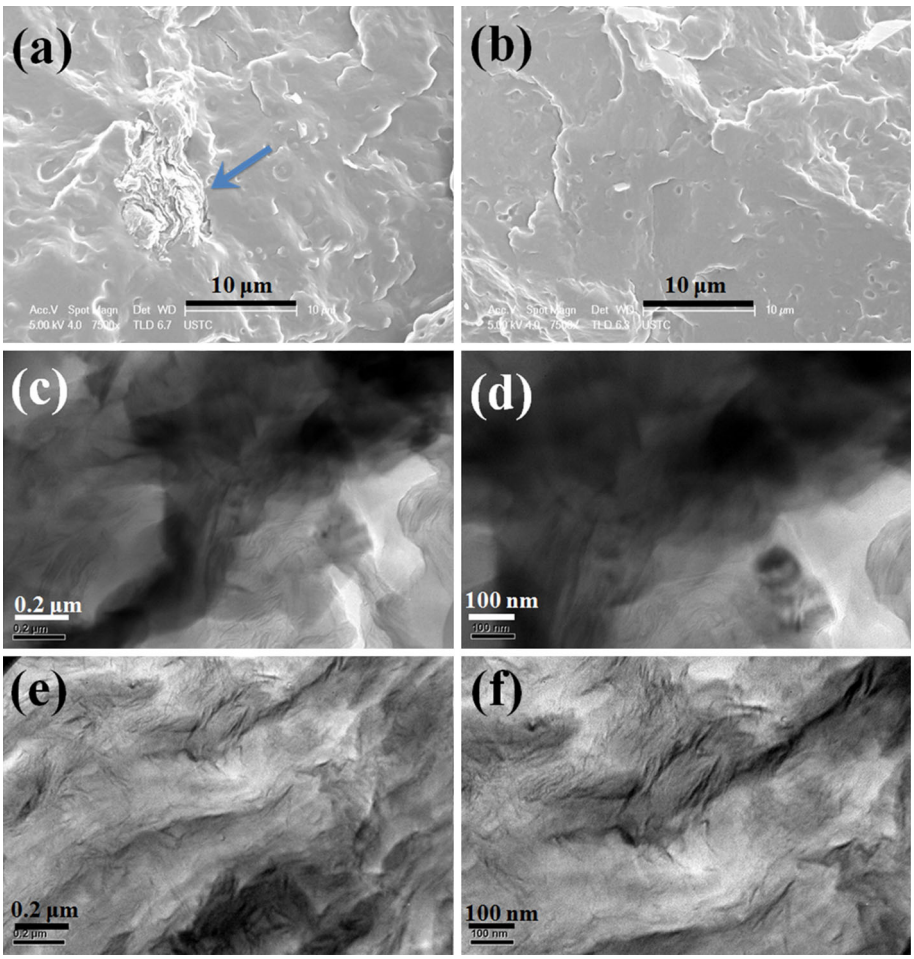

Fig. 9 SEM images of the freeze-fractured surface of **a** 2 GO/PP and **b** 2 FGO/PP; TEM images of the ultrathin slices of **c**, **d** 2 GO/PP and **e**, **f** 2 FGO/PP

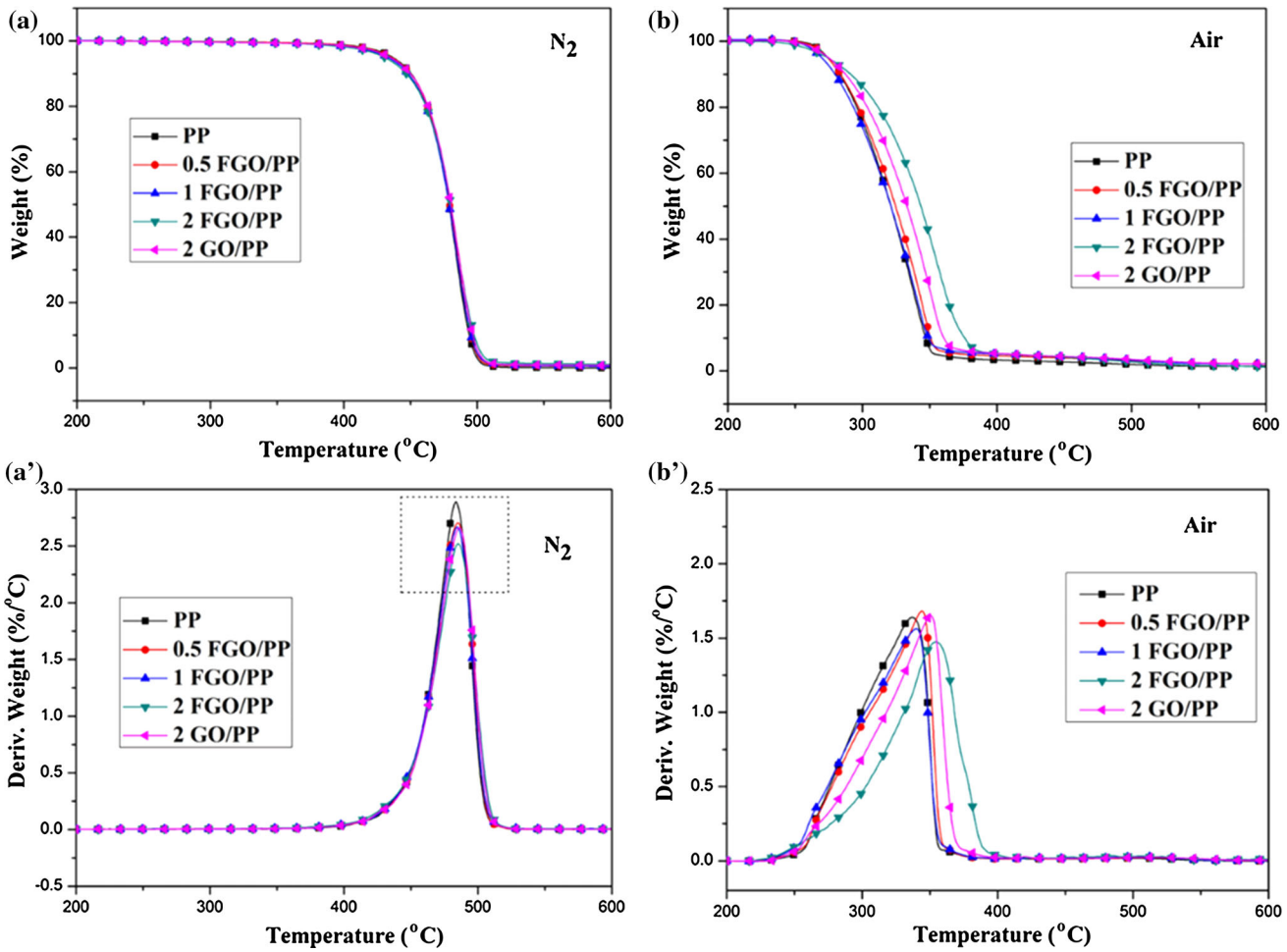

Fig. 10 TGA and DTG curves of PP and its composites under **a**, **a′** N_2 and **b**, **b′** air atmosphere

Table 1 TGA and cone calorimeter data of PP and its composites

Sample	$T_{initial}$ (°C)		T_{max} (°C)		TTI (s)	PHRR (kW/m^2)	THR (MJ/m^2)
	N_2	Air	N_2	Air			
PP	436	275	483	336	50	1044	101.4
0.5 FGO/PP	436	274	486	345	40	892	104.1
1 FGO/PP	433	270	485	341	37	834	100.6
2 FGO/PP	430	274	485	355	33	739	98.7
2 GO/PP	434	275	486	351	33	979	108.2

PP with two different magnifications are presented in Fig. 9c–f. As shown in Fig. 9c, d, the virgin GO is not homogeneously dispersed in the PP matrix and GO aggregates are observed, due to the poor compatibility. The TEM images of 2 FGO/PP exhibit a good dispersion morphology. In general, the FGO nanosheets are well dispersed throughout the matrix with intercalation and exfoliation microstructures (Fig. 9e, f). Upon the intercalation of MA molecules, the interlayer spacing of GO is enlarged and its surface characteristic is tailored. Thus, compared to the virgin GO, it is easier to achieve homogeneous dispersion of FGO in PP matrix.

Oxidative and non-oxidative thermal decomposition studies of PP and its composites were conducted using TGA under air and N_2 atmosphere, respectively. The TGA plots and the relevant data are presented in Fig. 10 and Table 1, respectively. The initial decomposition temperature ($T_{initial}$) in this work is defined as the temperature at 5 % mass loss. The temperature (T_{max}) and the value (MLR_{max}) of maximum weight loss rate are obtained from

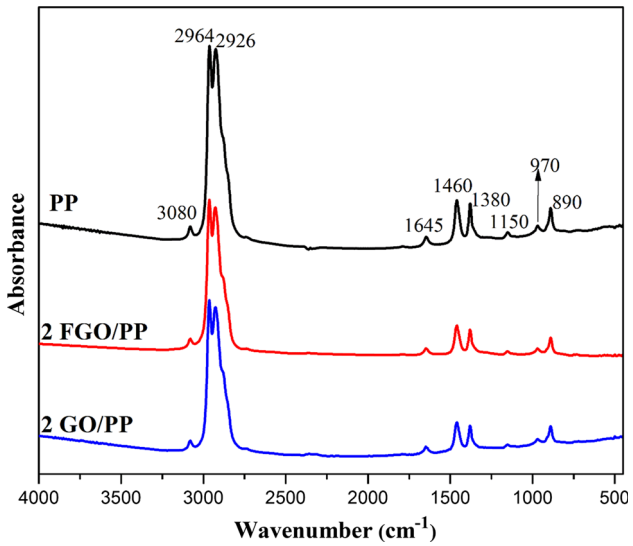

Fig. 11 FTIR absorption spectra of the pyrolysis products of PP, 2 FGO/PP, and 2 GO/PP at the maximum decomposition rate

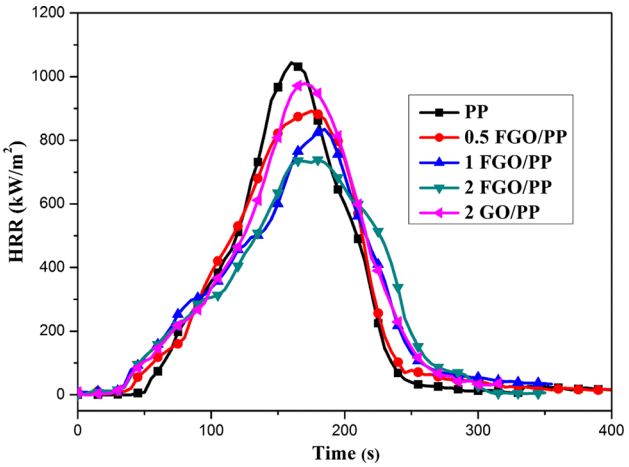

Fig. 12 HRR curves of PP and its composites

the differential thermogravimetric (DTG) curves. In comparison to neat PP, no obvious enhancement in thermal stability under N_2 atmosphere is achieved for PP composites. However, the MLR_{max} of FGO/PP nanocomposites gradually decreases with increasing loading of FGO. In addition, the MLR_{max} of 2 FGO/PP is less than that of 2 GO/PP. As evident from the TGA curves under air atmosphere, the PP composites exhibit similar thermal stability to neat PP. However, after 280 °C, the thermal stability of PP composites, especially 2 GO/PP and 2 FGO/PP, is improved. The T_{max} of 2 FGO/PP is 19 °C higher than that of neat PP, and 2 FGO/PP exhibits higher thermal-oxidative stability than 2 GO/PP. Furthermore, under air atmosphere, the MLR_{max} of 2 FGO/PP is also lower than that of 2 GO/PP. The good dispersion of FGO and the in situ formed g-C_3N_4 results in the enhancement of the thermal stability of 2 FGO/PP.

TG-IR technique was used to continuously monitor the evolution of pyrolysis products of PP and its composites during the thermal decomposition. Neat PP, 2 FGO/PP, and 2 GO/PP exhibit similar FTIR spectra of the volatile degradation products at the maximum decomposition rate, as shown in Fig. 11. The main gas decomposition products of PP and its composites are saturated hydrocarbons and unsaturated alkane [16]. The peaks at 2964, 2926, 1460, 1380, 1150, and 970 cm^{-1} in Fig. 11 are attributed to the saturated hydrocarbons [16]. The characteristic bands of unsaturated alkane appear at 3080, 1645, and 890 cm^{-1} [16]. Thus, GO and FGO have negligible influence on the thermal decomposition pathway of PP. These nanomaterials exhibit inert behavior under the anaerobic atmosphere.

Cone calorimetry is widely acknowledged as the most effective tool for evaluating the flammability of polymers. Heat release rate (HRR) curves of PP and its composites are shown in Fig. 12, and the combustion data, including time to ignition (TTI), peak heat release rate (PHRR), and total heat release (THR), are summarized in Table 1. Compared with neat PP, the graphene-based PP composites exhibit earlier ignition phenomenon, which is due to the enhanced heat absorption within the surface layer of these carbon nanomaterial-containing composites [16]. PHRR is regarded as one of the most important parameters to investigate the combustion behavior. The reduction in PHRR is an indicator for improving the flame retardancy. The PHRR values of FGO/PP composites decrease with increasing the loading of FGO. In comparison to neat PP, a 29 % decrease in PHRR is observed for the 2 FGO/PP nanocomposite. However, no marked reduction in PHRR is observed for 2 GO/PP. It is apparent that the FGO-based PP composite exhibits better flame retardant properties than those of GO/PP composite. Compared to neat PP, the addition of GO and FGO does not lead to the marked decrease in THR.

Digital photographs of the char residue of 2 GO/PP and 2 FGO/PP are shown in Fig. S1 in Supplementary Material. The fire char of 2 GO/PP is a powder-like product. However, the char residue with continuous structure and higher cover area is obtained for 2 FGO/PP, indicating the better protection effect. The graphitization degree of the char plays an important role in improving flame retardancy of polymers. The residual char with higher graphitization degree shows higher stability to thermal oxidation and better protection effects [51]. The ratio of D and G bands from Raman spectra is inversely proportional to graphitization degree [51]. Raman spectra of the residual char of 2 GO/PP and 2 FGO/PP after the cone tests are shown in

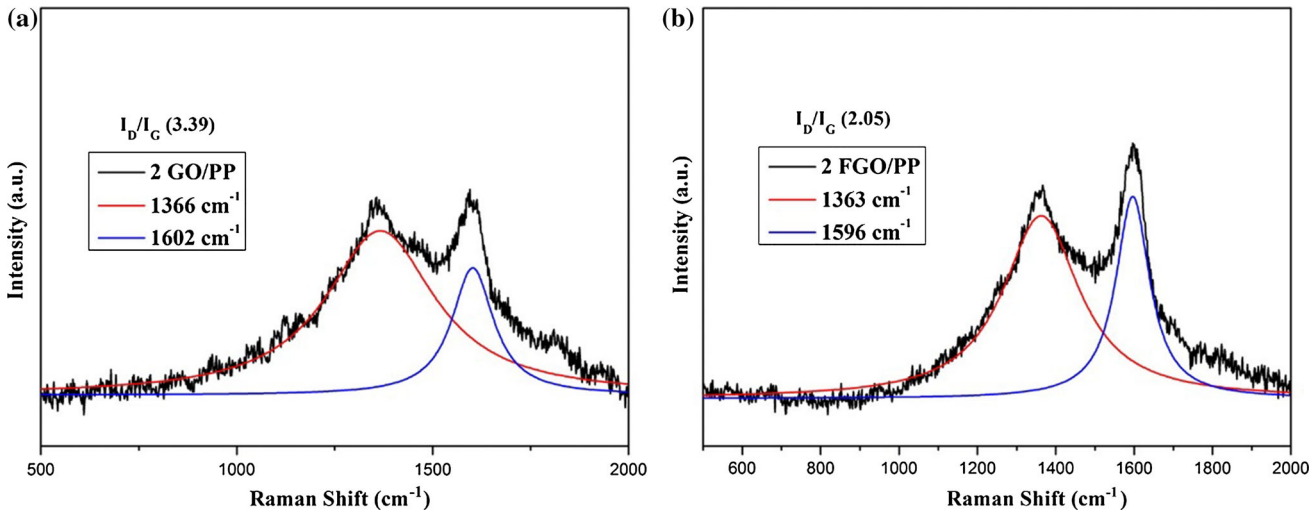

Fig. 13 Raman spectra of the char residue of **a** 2 GO/PP and **b** 2 FGO/PP

Fig. 13. The chemical structure of neat GO has been severely damaged during the combustion, resulting in the high value of I_D/I_G (3.39) and low graphitization degree. However, the I_D/I_G of the char of 2 FGO/PP (2.05) is slightly higher than that of the original FGO (1.87), owing to the protection of the in situ formed g-C_3N_4. That is to say, the g-C_3N_4 mitigates the destruction of GO structure during the combustion and improves the graphitization degree and thermal stability of the char.

Conclusions

In this study, GO was modified by a non-covalent approach to improving the dispersion in PP matrix and controlling the interfacial structure. The modifier of MA was coated on the GO nanosheets via the strong π–π attraction, hydrogen bonding, and electrostatic interactions. FGO/GO-based PP composites were prepared by an environmentally friendly approach, melt compounding method. FGO exhibited better dispersion in PP than did GO. The addition of FGO into PP matrix produced higher improvements in thermal stability and flame retardancy than those of GO/PP composite. Compared with neat PP and 2 GO/PP, the mass loss rate during the thermal decomposition and the heat release during the combustion were considerably decreased in 2 FGO/PP nanocomposite. The mechanism for these enhancements was clearly illuminated. In the confined microzone created by GO nanosheets, the sublimation of MA was greatly retarded and the GO acted as a template to improve the thermal condensation of MA into g-C_3N_4. The in situ formed g-C_3N_4 was coated on the graphene nanosheets, and it acted as a protective layer to improve the thermal stability of graphene. Meanwhile, the thermal stability of the g-C_3N_4 was also enhanced by the graphene nanosheets. Due to the presence of g-C_3N_4, the barrier performance of graphene was improved, resulting in the enhancement of thermal stability and flame retardant property of FGO/PP nanocomposites. This work demonstrated the importance of good dispersion of GO on the improvement in flame retardancy of polymers.

Acknowledgements The authors acknowledge the research grants from the National Natural Science Foundation of China (Grant No. 21374111), the Natural Science Foundation of Jiangsu Province (Grant No. BK20130369), and the Research Grants Council of the Hong Kong Special Administrative Region, China (Grant No. 9042047, CityU 11208914).

References

1. Du J, Cheng H-M (2012) The fabrication, properties, and uses of graphene/polymer composites. Macromol Chem Phys 213:1060–1077
2. Zhang H-B, Zheng W-G, Yan Q, Jiang Z-G, Yu Z-Z (2012) The effect of surface chemistry of graphene on rheological and electrical properties of polymethylmethacrylate composites. Carbon 50:5117–5125
3. Tripathi SN, Saini P, Gupta D, Choudhary V (2013) Electrical and mechanical properties of PMMA/reduced graphene oxide nanocomposites prepared via in situ polymerization. J Mater Sci 48:6223–6232. doi:10.1007/s10853-013-7420-8
4. Kim H, Abdala AA, Macosko CW (2010) Graphene/polymer nanocomposites. Macromolecules 43:6515–6530
5. Kim H, Kobayashi S, AbdurRahim MA, Zhang MJ, Khusainova A, Hillmyer MA, Abdala AA, Macosko CW (2011) Graphene/polyethylene nanocomposites: effect of polyethylene functionalization and blending methods. Polymer 52:1837–1846
6. Salavagione HJ, Martínez G, Ellis G (2011) Recent advances in the covalent modification of graphene with polymers. Macromol Rapid Commun 32:1771–1789
7. Yuan BH, Bao CL, Song L, Hong NN, Liew KM, Hu Y (2014) Preparation of functionalized graphene oxide/polypropylene

nanocomposite with significantly improved thermal stability and studies on the crystallization behavior and mechanical properties. Chem Eng J 237:411–420
8. Singh V, Joung D, Zhai L, Das S, Khondaker SI, Seal S (2011) Graphene based materials: past, present and future. Prog Mater Sci 56:1178–1271
9. Kalaitzidou K, Fukushima H, Drzal LT (2007) Mechanical properties and morphological characterization of exfoliated graphite-polypropylene nanocomposites. Compos Part A 38:1675–1682
10. Ye S, Feng J (2013) A new insight into the in situ thermal reduction of graphene oxide dispersed in a polymer matrix. Polym Chem 4:1765–1768
11. Zhu JH, Chen MJ, He QL, Shao L, Wei SY, Guo ZH (2013) An overview of the engineered graphene nanostructures and nanocomposites. RSC Adv 3:22790–22824
12. Ran SY, Guo ZH, Han LG, Fang ZP (2014) Effect of Friedel-Crafts reaction on the thermal stability and flammability of high-density polyethylene/brominated polystyrene/graphene nanoplatelet composites. Polym Int 63:1835–1841
13. Han Y, Wu Y, Shen M, Huang X, Zhu J, Zhang X (2013) Preparation and properties of polystyrene nanocomposites with graphite oxide and graphene as flame retardants. J Mater Sci 48:4214–4222. doi:10.1007/s10853-013-7234-8
14. Bao CL, Song L, Wilkie CA, Yuan BH, Guo YQ, Hu Y, Gong XL (2012) Graphite oxide, graphene, and metal-loaded graphene for fire safety applications of polystyrene. J Mater Chem 22:16399–16406
15. Dittrich B, Wartig KA, Hofmann D, Mulhaupt R, Schartel B (2013) Flame retardancy through carbon nanomaterials: carbon black, multiwall nanotubes, expanded graphite, multi-layer graphene and graphene in polypropylene. Polym Degrad Stabil 98:1495–1505
16. Dittrich B, Wartig KA, Hofmann D, Mulhaupt R, Schartel B (2013) Carbon black, multiwall carbon nanotubes, expanded graphite and functionalized graphene flame retarded polypropylene nanocomposites. Polym Adv Technol 24:916–926
17. Ran SY, Chen C, Guo ZH, Fang ZP (2014) Char barrier effect of graphene nanoplatelets on the flame retardancy and thermal stability of high-density polyethylene flame-retarded by brominated polystyrene. J Appl Polym Sci 131:40520
18. Song PA, Yu YM, Zhang T, Fu SY, Fang ZP, Wu Q (2012) Permeability, viscoelasticity, and flammability performances and their relationship to polymer nanocomposites. Ind Eng Chem Res 51:7255–7263
19. Huang GB, Wang SQ, Song PA, Wu CL, Chen SQ, Wang X (2014) Combination effect of carbon nanotubes with graphene on intumescent flame-retardant polypropylene nanocomposites. Compos Part A 59:18–25
20. Gong J, Niu R, Liu J, Chen XC, Wen X, Mijowska E, Sun ZY, Tang T (2014) Simultaneously improving the thermal stability, flame retardancy and mechanical properties of polyethylene by the combination of graphene with carbon black. RSC Adv 4:33776–33784
21. Dittrich B, Wartig KA, Mulhaupt R, Schartel B (2014) Flame-retardancy properties of intumescent ammonium poly(phosphate) and mineral filler magnesium hydroxide in combination with graphene. Polymers 6:2875–2895
22. Lorenzetti A, Besco S, Hrelja D, Roso M, Gallo E, Schartel B, Modesti M (2013) Phosphinates and layered silicates in charring polymers: the flame retardancy action in polyurethane foams. Polym Degrad Stabil 98:2366–2374
23. Wu GM, Schartel B, Bahr H, Kleemeier M, Yu D, Hartwig A (2012) Experimental and quantitative assessment of flame retardancy by the shielding effect in layered silicate epoxy nanocomposites. Combust Flame 159:3616–3623
24. Schartel B, Weiss A, Sturm H, Kleemeier M, Hartwig A, Vogt C, Fischer RX (2011) Layered silicate epoxy nanocomposites: formation of the inorganic-carbonaceous fire protection layer. Polym Adv Technol 22:1581–1592
25. Acik M, Lee G, Mattevi C, Pirkle A, Wallace RM, Chhowalla M, Cho K, Chabal Y (2011) The role of oxygen during thermal reduction of graphene oxide studied by infrared absorption spectroscopy. J Phys Chem C 115:19761–19781
26. Kim H, Macosko CW (2008) Morphology and properties of polyester/exfoliated graphite nanocomposites. Macromolecules 41:3317–3327
27. Hummers WS, Offeman RE (1958) Preparation of graphitic oxide. J Am Chem Soc 80:1339
28. Yuan BH, Bao CL, Qian XD, Wen PY, Xing WY, Song L, Hu Y (2014) A facile approach to prepare graphene via solvothermal reduction of graphite oxide. Mater Res Bull 55:48–52
29. Liang W, Chen X, Sa Y, Feng Y, Wang Y, Lin W (2012) Graphene oxide as a substrate for Raman enhancement. Appl Phys A 109:81–85
30. León V, Quintana M, Herrero MA, Fierro JLG, Adl Hoz, Prato M, Vázquez E (2011) Few-layer graphenes from ball-milling of graphite with melamine. Chem Commun 47:10936–10938
31. Leon V, Rodriguez AM, Prieto P, Prato M, Vazquez E (2014) Exfoliation of graphite with triazine derivatives under ball-milling conditions: preparation of few-layer graphene via selective noncovalent interactions. ACS Nano 8:563–571
32. Yuan BH, Bao CL, Qian XD, Jiang SH, Wen PY, Xing WY, Song L, Liew KM, Hu Y (2014) Synergetic dispersion effect of graphene nanohybrid on the thermal stability and mechanical properties of ethylene vinyl acetate copolymer nanocomposite. Ind Eng Chem Res 53:1143–1149
33. Costa L, Camino G (1988) Thermal-behavior of melamine. J Therm Anal 34:423–429
34. Park S, Lee KS, Bozoklu G, Cai W, Nguyen ST, Ruoff' RS (2008) Graphene oxide papers modified by divalent ions—enhancing mechanical properties via chemical cross-linking. ACS Nano 2:572–578
35. Fan X, Peng W, Li Y, Li X, Wang S, Zhang G, Zhang F (2008) Deoxygenation of exfoliated graphite oxide under alkaline conditions: a green route to graphene preparation. Adv Mater 20:4490–4493
36. Yang S, Yue W, Huang D, Chen C, Lin H, Yang X (2012) A facile green strategy for rapid reduction of graphene oxide by metallic zinc. RSC Adv 2:8827–8832
37. Gao J, Hu M, Dong Y, Li RKY (2013) Graphite-nanoplatelet-decorated polymer nanofiber with improved thermal, electrical, and mechanical properties. ACS Appl Mater Interfaces 5:7758–7764
38. Liang J, Huang Y, Zhang L, Wang Y, Ma Y, Guo T, Chen Y (2009) Molecular-level dispersion of graphene into poly(vinyl alcohol) and effective reinforcement of their nanocomposites. Adv Funct Mater 19:2297–2302
39. Sierra U, Álvarez P, Santamaría R, Granda M, Blanco C, Menéndez R (2014) A multi-step exfoliation approach to maintain the lateral size of graphene oxide sheets. Carbon 80:830–832
40. Petit C, Bandosz TJ (2009) Graphite oxide/polyoxometalate nanocomposites as adsorbents of ammonia. J Phys Chem C 113:3800–3809
41. Bourlinos AB, Gournis D, Petridis D, Szabo T, Szeri A, Dekany I (2003) Graphite oxide: chemical reduction to graphite and surface modification with primary aliphatic amines and amino acids. Langmuir 19:6050–6055
42. Zhai H-S, Cao L, Xia X-H (2013) Synthesis of graphitic carbon nitride through pyrolysis of melamine and its electrocatalysis for oxygen reduction reaction. Chin Chem Lett 24:103–106
43. Sun H, Zhou G, Wang Y, Suvorova A, Wang S (2014) A new metal-free carbon hybrid for enhanced photocatalysis. ACS Appl Mater Interfaces 6:16745–16754

44. Yuan B, Bao C, Qian X, Song L, Tai Q, Liew KM, Hu Y (2014) Design of artificial nacre-like hybrid films as shielding to mitigate electromagnetic pollution. Carbon 75:178–189
45. Hu SW, Yang LW, Tian Y, Wei XL, Ding JW, Zhong JX, Chu PK (2015) Simultaneous nanostructure and heterojunction engineering of graphitic carbon nitride via in situ Ag doping for enhanced photoelectrochemical activity. Appl Catal B 163:611–622
46. Xu H, Song Y, Song Y, Zhu J, Zhu T, Liu C, Zhao D, Zhang Q, Li H (2014) Synthesis and characterization of g-C_3N_4/Ag_2CO_3 with enhanced visible-light photocatalytic activity for the degradation of organic pollutants. RSC Adv 4:34539–34547
47. Li Y, Sun Y, Dong F, Ho W-K (2014) Enhancing the photocatalytic activity of bulk g-C_3N_4 by introducing mesoporous structure and hybridizing with graphene. J Colloid Interf Sci 436:29–36
48. Bagri A, Mattevi C, Acik M, Chabal YJ, Chhowalla M, Shenoy VB (2010) Structural evolution during the reduction of chemically derived graphene oxide. Nat Chem 2:581–587
49. Pei S, Cheng H-M (2012) The reduction of graphene oxide. Carbon 50:3210–3228
50. Liu L, Shi Y, Yu B, Tai Q, Wang B, Feng X, Liu H, Wen P, Yuan B, Hu Y (2015) Preparation of layered graphitic carbon nitride/montmorillonite nanohybrids for improving thermal stability of sodium alginate nanocomposites. RSC Adv 5:11761–11765
51. Ma HY, Tong LF, Xu ZB, Fang ZP (2007) Synergistic effect of carbon nanotube and clay for improving the flame retardancy of ABS resin. Nanotechnology 18:375602